

# PHOTONICS Research

## Stimulated emission at 1.54 $\mu\text{m}$ from erbium/oxygen-doped silicon-based light-emitting diodes

JIN HONG,<sup>1,†</sup>  HUIMIN WEN,<sup>2,†</sup> JIAJING HE,<sup>2</sup> JINGQUAN LIU,<sup>2</sup> YAPING DAN,<sup>2,5</sup>  JENS W. TOMM,<sup>3</sup>   
FANGYU YUE,<sup>1,6</sup> JUNHAO CHU,<sup>1,4</sup> AND CHUNGANG DUAN<sup>1,7</sup>

<sup>1</sup>Key Laboratory of Polar Materials and Devices, Ministry of Education, East China Normal University, Shanghai 200241, China

<sup>2</sup>National Key Laboratory of Science and Technology on Micro/Nano Fabrication Laboratory, Department of Micro/Nano Electronics, University of Michigan-Shanghai Jiao Tong University Joint Institute, Shanghai Jiao Tong University, Shanghai 200240, China

<sup>3</sup>Max-Born-Institut für Nichtlineare Optik und Kurzzeitspektroskopie, 12489 Berlin, Germany

<sup>4</sup>National Laboratory for Infrared Physics, Shanghai Institute of Technical Physics, Chinese Academy of Sciences, Shanghai 200083, China

<sup>5</sup>e-mail: yaping.dan@sjtu.edu.cn

<sup>6</sup>e-mail: fyyue@ee.ecnu.edu.cn

<sup>7</sup>e-mail: cgduan@clpm.ecnu.edu.cn

Received 16 December 2020; revised 7 February 2021; accepted 7 February 2021; posted 8 February 2021 (Doc. ID 417090); published 21 April 2021

Silicon-based light sources, including light-emitting diodes (LEDs) and laser diodes (LDs) for information transmission, are urgently needed for developing monolithic integrated silicon photonics. Silicon with erbium ions ( $\text{Er}^{3+}$ ) doped by ion implantation is considered a promising approach, but it suffers from an extremely low quantum efficiency. Here we report an electrically pumped superlinear emission at 1.54  $\mu\text{m}$  from Er/O-doped silicon planar LEDs, which are produced by applying a new deep cooling process. Stimulated emission at room temperature is realized with a low threshold current of  $\sim 6$  mA ( $\sim 0.8$  A/cm<sup>2</sup>). Time-resolved photoluminescence and photocurrent results have revealed the complex carrier transfer dynamics by relaxing electrons from the Si conduction band to the  $\text{Er}^{3+}$  ion. This picture differs from the frequently assumed energy transfer via electron-hole pair recombination of the silicon host. Moreover, the amplified emission from the LEDs is likely due to a quasi-continuous Er/O-related donor band created by the deep cooling technique. This work paves the way for fabricating superluminescent diodes or efficient LEDs at communication wavelengths based on rare-earth-doped silicon. © 2021 Chinese Laser Press

<https://doi.org/10.1364/PRJ.417090>

### 1. INTRODUCTION

Silicon/Si-based light sources, including lasers at telecommunication wavelengths, are the bottleneck for the heterogeneous integration of photonics with complementary metal-oxide-semiconductor circuits [1–6]. Ion implantation of erbium (Er) (often with oxygen) into Si is believed to be one of the most promising approaches to create Si-based light-emitting devices (LEDs) at 1.54  $\mu\text{m}$  [7–15]. However, the reported quantum efficiencies are extremely low ( $\approx 0.01\%$ ) at room temperature, mainly due to strong nonradiative recombination caused by the comparably large Er-related precipitates formed during the cooling process in the standard rapid thermal annealing (RTA) [3,15–17]. Recently, the efficiency has been substantially improved by introducing a deep cooling (DC) technique [11] that can effectively mitigate the Er precipitation created during the RTA process. LEDs with a perpendicular emission structure based on the obtained material achieved a record external quantum efficiency of  $\sim 0.8\%$  at room temperature [11].

Here, by optimizing the implantation of Er and O, the DC procedure, and the Si-based LED structure with a planar emission geometry, a near-unity quantum yield (or  $\sim 100\%$  slope efficiency) of the photoluminescence (PL) in Er-doped Si is reached. Moreover, a superlinearly growing electroluminescence (EL) is obtained with a slope efficiency beyond 2 even at room temperature. The low threshold of  $\sim 6$  mA ( $\sim 0.8$  A/cm<sup>2</sup>) [18,19], the superlinear EL integral intensity [20–22], the narrowing full width at half-maximum (FWHM) [23,24], and the Gaussian-like spatial emission distribution [25–29] confirm the presence of stimulated emission involving transitions related to the  $\text{Er}^{3+}$  [30–33]. Time-resolved PL (TR-PL) and photocurrent (PC) measurements reveal the relaxation dynamics of the non-equilibrium carriers from the Si host to the  $\text{Er}^{3+}$  precipitates. The hot nonequilibrium carriers in Si first cross the intravalley barrier (e.g.,  $\Gamma$  or L point in  $k$ -space if the laser energy is high enough) with a time constant of  $\sim 110$  ps to the bottom of the indirect conduction band (CB) (or the  $\Delta_{1c}$  point) [34,35].

The excess carriers further decay from the CB bottom to the evenly distributed Er/O-related complexes that act as a quasi-continuous donor band with a decay time of  $\sim 30$  ps. Within this donor band, the carriers resonantly excite (i.e., transfer the energy of carriers by nonradiative recombination to) the  $\text{Er}^{3+}$ -4f electrons to emit at  $\sim 1.54 \mu\text{m}$  ( $^4\text{I}_{13/2} \rightarrow ^4\text{I}_{15/2}$ ).

## 2. MATERIALS AND METHODS

### A. Sample Fabrication

Float zone intrinsic Si (100) wafers (resistivity:  $\geq 10 \text{ k}\Omega \cdot \text{cm}$ ; thickness:  $500 \pm 20 \mu\text{m}$ ; Suzhou Resemi Semiconductor Co., Ltd, China) were used. Er and O ions were implanted with an injection energy and dose of 200 keV and  $4 \times 10^{15} \text{ cm}^{-2}$ , and 32 keV and  $10^{16} \text{ cm}^{-2}$ , respectively, at the Institute of Semiconductors, Chinese Academy of Sciences, China. After that, the Er/O-implanted Si samples were cleaned with ethanol and deionized water, and then they were immersed in a piranha solution (sulfuric acid:30% hydrogen peroxide = 3:1) for 30 min at  $90^\circ\text{C}$ , followed by drying with a high-purity nitrogen (99.99%) stream. To form a planar p-n junction, we further implanted boron (B) and phosphorus (P) dopants into these Si samples (B: 30 keV and  $2.2 \times 10^{14} \text{ cm}^{-2}$ ; P: 80 keV and  $2.2 \times 10^{14} \text{ cm}^{-2}$ ). They have a similar peak concentration located  $\sim 80$  nm below the surface, which matches the peak depth of the Er in Si. Then 200 nm thick  $\text{SiO}_2$  films were deposited on the Er/O-implanted Si samples by reactive magnetron sputtering (Delton multitarget magnetic control sputtering system, AEMD, SJTU). A DC process was performed to activate the Er/O, B, and P dopants at the same time via an upgraded dilatometer (DIL 805A, TA Instruments) [11], where the samples were annealed at  $950^\circ\text{C}$  for 5 min by means of copper-coil-based electromagnetic heating and followed by a flush of high-purity He (99.999%) gas cooled in liquid  $\text{N}_2$  (77 K). Detailed descriptions can be found in our previous work in Ref. [11].

A pair of coaxial electrodes was prepared by UV photolithography (MDA-400M, MIDAS) and metal film deposition (Nexdep, Angstrom Engineering Inc.). The internal electrode is in contact with the p-type boron doping region, and the external electrode in contact with the n-type P region. The schematic representations of the fabrication procedure to form Er/O-doped Si samples and LEDs are shown in Fig. 6 in Appendix A. All the microfabrication processes were performed with home-built devices at the Center for Advanced Electronic Materials and Devices, Shanghai Jiao Tong University. After the Al metal wire bonding (7476D, West Bond), the devices were integrated on a printed circuit board. The  $I-V$  curves were taken using a digital sourcemeter (Keithley 2400) controlled by a LabVIEW script.

### B. Optical Characterizations

A Fourier transform infrared (FTIR) spectrometer (Vertex 80v, Bruker) was employed to measure transmission, reflectance, steady-state PL and EL, and PC spectra. The focused 405 nm emission from a continuous-wave (cw) laser diode (MLL-III-405, CNI, Changchun, China) with a maximum excitation power of  $\sim 160$  mW was employed as the excitation source. The effective excitation power on the sample surface was calibrated by referring to the 405 nm transmission and reflectance

of the samples at different temperatures. Different optical filters including notch filters, neutral density filters, and long-pass filters were utilized for avoiding the influence of the excitation during the excitation-power-dependent PL measurements. For EL measurements, cw and pulsed [with a nanosecond (ns) to microsecond ( $\mu\text{s}$ ) pulse duration and a repetition rate of  $\sim 10^4$  Hz] currents were injected into the structures. For PC measurements, a low-noise current preamplifier (SRS SR570) was employed for recording the defect-related PC signal below the band gap of Si.

TR-PL was carried out in order to determine the nonequilibrium carrier lifetime related to  $\text{Er}^{3+}$ . This was implemented by milliwatt (mW) excitation with a 405 nm emitting diode laser being operated at 3 kHz as the excitation source, a fast InGaAs photodiode, and a gigahertz (GHz) sampling oscilloscope (Agilent MSO9404A) for data accumulation and read-out. Simultaneously, the PL decay curve was cross-checked by a luminescence spectrometer. TR-PL at an 80 MHz repetition rate was implemented by using a Tsunami Ti:sapphire laser (760 or 380 nm by using second harmonic, spot size  $\sim 100 \mu\text{m}$ ) with 80 fs excitation pulses. The maximum energy density per pulse amounts to 57 and  $3.4 \mu\text{J}/\text{cm}^2$  at 780 and 390 nm, respectively. Detection was made by a Hamamatsu C5680 streak camera with S1 photocathode operated in synchro-scan mode. The overall temporal resolution of the setup ( $1/e$  decay of an 80 fs pulse) is better than 10 ps. In all setups the samples were mounted on the cold head of a helium closed-cycle cooler. This allows for temperature adjustment from 4 K to ambient.

Near infrared EL imaging from the Er/O-Si LEDs was obtained at room temperature under an optical microscope (BX53M, Olympus) equipped with a near-infrared camera (C12471-03, Hamamatsu). The recorded video is provided in Appendix B (see Visualization 1).

## 3. RESULTS AND DISCUSSION

### A. Precharacterization by PL Measurements

Room-temperature PL spectra of Er/O-doped Si at different excitation powers ( $\lambda = 405 \text{ nm}$ ; 3.06 eV) are shown in Fig. 1(a).  $\text{Er}^{3+}$  emission at  $\sim 1.54 \mu\text{m}$  ( $\sim 0.81$  eV; marked with A) is observed and becomes more pronounced when the excitation power increases. Besides the main emission peak A, there is a side shoulder and a broad tail at the high-energy side denoted as B (at  $\sim 0.82$  eV) and C (even beyond the band gap of Si), respectively (see inset). The shoulder B is ascribed to the  $\text{Er}^{3+}$ -related states [12], and the tail C is related to the Er/O-doping induced defect centers in the band gap of Si. No shape change of the emission occurs when the excitation power is higher than  $\sim 5$  mW. The integral intensity of the three specified emission bands A, B, and C shows a slope efficiency of near unity ( $S \approx 0.93$ ) within 2 orders of magnitude of excitation power [Fig. 1(b) in a log-log scale]. It characterizes the quasi-free carrier recombination and the high internal quantum yield of  $\text{Er}^{3+}$  without efficient (Auger or thermally related) nonradiative recombination, even at room temperature. At low temperature, the PL efficiency is enhanced as expected by suppressing the Shockley-Read-Hall recombination [11,15]. What is interesting is that the shoulder B and tail C are

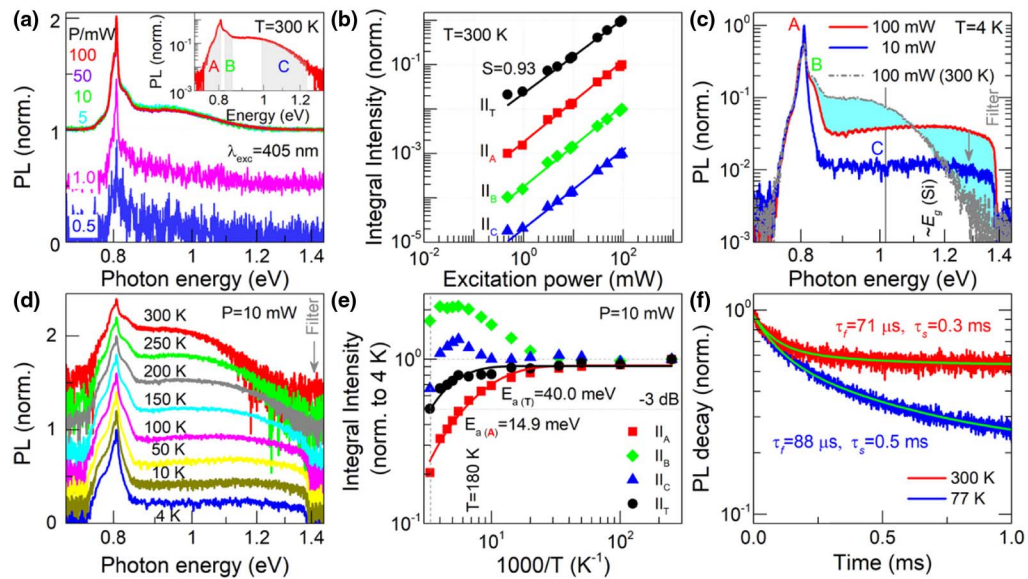


**Fig. 1.** PL spectra. (a) Room-temperature PL spectra from the Er/O-doped Si at different excitation powers ( $P$ ). PL curves are tentatively divided into three parts, marked by A, B and C, as shown in the inset. (b) Excitation power dependence of PL integral intensity (II) at 300 K. (c) PL spectra at  $P = 10$  mW (blue curve) and 100 mW (red curve) at 4 K. The room-temperature PL result at  $P = 100$  mW (gray curve) is also given for comparison. (d) PL spectra at different temperatures ( $P = 10$  mW). (e) Arrhenius plot of normalized PL integral intensity versus inversed temperature. (f) PL decay curves at 77 and 300 K together with the fitting results.

evident and can be strengthened in comparison with the main peak A as the excitation power increases; see the PL spectra (4 K) at 10 mW and 100 mW in Fig. 1(c). It is clear by comparing the curve at 4 K with that at 300 K that elevated temperatures have strong influence on the emission processes in B and C. Figure 1(d) (normalized to peak A) demonstrates that the long tail C is substantially narrowed by shifting the edge emission toward the long-wavelength side upon increase of temperature; also see the two-colored areas in Fig. 1(c). The narrowing of the tail C unlikely originates from the temperature-dependent absorptivity of excitation light ( $\lambda = 405$  nm), as this effect has been taken into account in our measurements (see Fig. 8 in Appendix C). Instead, it likely comes from the temperature-driven redistribution of excess carriers from the high-energy states in the Si CB to those within the Si band gap (see more discussions later). This narrowing results in a relatively stronger emission for both shoulder B and tail C as shown in Fig. 1(d).

To have a deeper insight into the above process, the integral intensities of the main peak A, the side shoulder B, and the tail C are normalized to their integral intensity at 4 K. The normalized integral intensities are shown in the Arrhenius plot in Fig. 1(e). While the main peak A quenches monotonously with increase of temperature, emissions of B and C first increase and then decrease at a critical temperature point of  $\sim 180$  K ( $\sim 15.5$  meV). Moreover, the total integral PL intensity also shows a monotonous decrease but with a relatively low temperature-quenching rate at 300 K (still  $\sim 50\%$  of 4 K, i.e., with a decrease of 3 dB). This means that excitons transfer between the states, which are involved in the generation of the emission bands A, B, and C, without being affected by strong temperature-dependent nonradiative recombination. Based on the evolutions in Fig. 1(e), an activation energy of

$\sim 14.9$  meV can be extracted for the main peak A (rather close to the phonon energy of  $\sim 15.5$  meV) [15] and one of  $\sim 40.0$  meV for the total emission. Figure 1(f) shows the PL decay of the  $1.54 \mu\text{m}$  emission at 300 K and 77 K for an excitation power of  $\sim 20 \text{ W/cm}^2$ . The transient PL decays following a biexponential function with a slow ( $0.5 \text{ ms}|_{77 \text{ K}}$ ,  $0.3 \text{ ms}|_{300 \text{ K}}$ ) and a fast ( $88 \mu\text{s}|_{77 \text{ K}}$ ,  $71 \mu\text{s}|_{300 \text{ K}}$ ) component. The slow one is the lifetime of  $\text{Er}^{3+}$  spontaneous emission, slightly shorter than the  $\sim$ millisecond (ms) lifetime of the  $\text{Er}^{3+}$  in Refs. [11,36]. The fast one could be attributed to the carrier relaxation between the sublevels of  $^4\text{I}_{13/2}$ , which will be further discussed later.

## B. Electrically Pumped Stimulated Emission

A lateral LED structure based on the DC-processed Er/O-doped Si structure is fabricated with a planar emission geometry (in contrast to our previous perpendicular structure) [11] [Fig. 2(a)]. We separately implanted boron and phosphorus into the Er/O-Si samples both with a peak concentration of  $10^{19} \text{ cm}^{-3}$ , forming a coaxial p-n junction diode on the Si surface [see Figs. 7(a) and 7(b) in Appendix A]. The DC process was then applied to activate the Er/O, B, and P dopants (see Section 2.A). A rectifying current versus voltage ( $I - V$ ) curve was observed [see Fig. 7(c) in Appendix A]. Figure 2(b) shows the EL spectra of the LED at different injection currents (at 300 K). Notice that the EL is similar in spectral shape to the PL from the Er/O-activated Si except that the tail C is weaker and cut off at the Si band gap; see the curves at the bottom of Fig. 2(c). With the injection current increase, the emission signal at  $\sim 0.81 \text{ eV}$  becomes clearer with the feature of the  $\text{Er}^{3+}$  emission at  $\sim 1.54 \mu\text{m}$ , and it simultaneously narrowed first and then broadened. The EL cutoff at the Si band gap (see the blue vertical line) is due to the fact that electrons



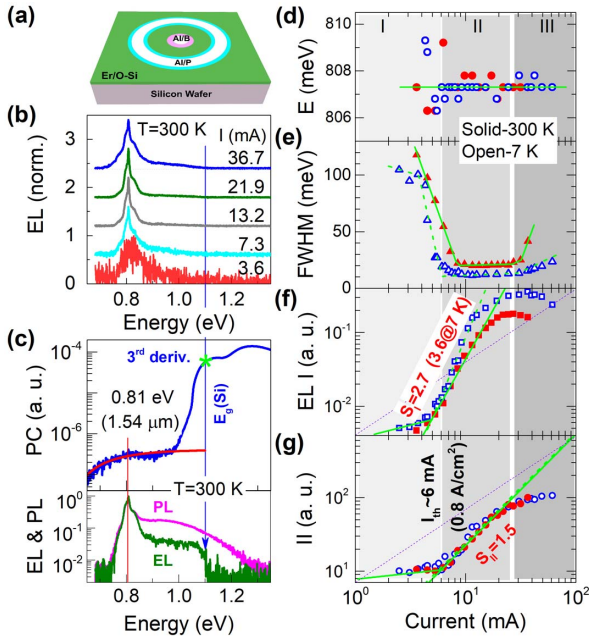


**Fig. 2.** EL spectra and analysis. (a) Schematic illustration of the LED structure. (b) Current-dependent EL spectra at 300 K. (c) PC spectrum at 300 K (upper panel). The star “\*” marks the maximum of the third-order derivative and the blue line  $E_g(\text{Si}) = 1.10$  eV. The PC shoulder at  $\sim 0.81$  eV is from the Er-related defects. The lower panel shows the EL and PL spectra of the LED at 300 K. (d)–(g) Current dependence of the EL peak energy, FWHM, intensity, and integrated intensity, respectively, at 300 K (red) and 7 K (blue). The green lines are guides to the eyes.

can be continuously electrically pumped to the CB bottom. In PL, electrons can be excited to high-energy states in the CB, resulting in a long emission tail well beyond the Si band gap.

To further clarify the energetic structure in the LEDs, we recorded the short-circuit PC spectra at 300 K under light illumination from 0.6 to 1.3 eV in photon energy as shown in Fig. 2(c). The third-order derivative of the curve sets the cutoff at  $\sim 1.1$  eV, which corresponds to the Si band gap  $E_g$ . It is necessary to point out that around 0.1 eV below the Si band gap, the PC reaches a plateau after an exponential decline by 2 orders of magnitude, which extends to  $\sim 0.6$  eV before it drops below the background noise. This PC plateau roughly lies in the same spectral range of the broad EL band, and it should come from the Er-related defect (including  $\text{Er}^{3+}$ -4f degenerated) states [37]. Taking into account the PC and EL bands from 0.7 to 1.1 eV, this implies that a quasi-continuous band from 0.7 eV above the valence band (VB) to the bottom of (or even above) the CB is formed.

Figures 2(d) and 2(e) show the main peak positions and FWHMs as functions of the injection current at 300 and 7 K. It can be observed that the main emission peak at  $1.54 \mu\text{m}$  is almost independent of the injection current, whereas the FWHM gives a visible reduction until the current approaches  $\sim 10$  mA. After a saturation region, the FWHM starts to broaden again when the injection current is higher than  $\sim 30$  mA. Moreover, in Figs. 2(f) and 2(g), as the injection current ramps up, the peak intensity and integral intensity

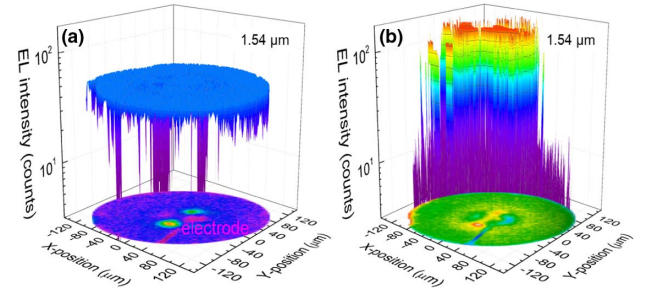


**Fig. 3.** Spatially resolved intensity distribution at the emitting surface of the LED at  $1.54 \mu\text{m}$  (a) below and (b) above the threshold current. The emission imaging of the surface is also shown at the bottom for comparison. The imaging region of EL is the area between two electrodes.

distinctively show a sublinear increase followed by superlinear ramp with a slope of  $S \approx 2.7$  at 300 K ( $\sim 3.6$  at 7 K) and  $S \approx 1.5$  at 300 K (almost the same at 7 K), respectively. A well-pronounced threshold is observed at  $\sim 6$  mA or  $0.8 \text{ A/cm}^2$  [refer to the integral intensity in Fig. 2(g)]. These features, along with the visible reduction of FWHM, suggest that amplified spontaneous [20,22,23] (or stimulated [32,33]) emission occurs in our Si LEDs. Clearly, the LED device operates in three different modes and transits sequentially from Mode I to II and to III as the current increases [see Figs. 2(d)–2(g)], in which Mode I represents the transition from spontaneous to amplified spontaneous emission; Mode II is the typical stimulated radiation with a distinctive superlinearity of the peak and integral intensity; and Mode III is the one in which the radiation recombination starts to be suppressed by the thermal effect of high injection current ( $\geq 30$  mA).

The emission cross section can be thus estimated by the following equation [29,38]:

$$\sigma_{\text{em}} = \sqrt{\ln\left(\frac{2}{\pi}\right)} (\lambda^4 / 4\pi c n^2 \tau w), \quad (1)$$

where  $c$  is the light speed,  $n$  is the refractive index (3.47),  $\tau$  is lifetime ( $\sim 70 \mu\text{s}$ ),  $w$  is the FWHM ( $\sim 0.10 \mu\text{m}$ ), and  $\lambda$  is the emission wavelength ( $1.54 \mu\text{m}$ ). Its maximum is approximately  $\sigma_{\text{em}} = 1.4 \times 10^{-19} \text{ cm}^2$ , which is almost double the value for the  $\text{Er}^{3+}$  in nanocrystal-Si sensitized silica ( $8.0 \times 10^{-20} \text{ cm}^2$ ) [15,21].

Figure 3 shows the spatially resolved emission intensity of the LED surface as taken by an InGaAs camera. At an injection current lower than the threshold [Fig. 3(a)], the emission is weak and uniformly distributed across the entire emitter surface ( $300 \mu\text{m}$  in diameter) except for the region close to the center electrode (see the two-dimensional image at the bottom), which is heated up. When the injection current is higher than the threshold, the emission is strongly enhanced with a maximum in the LED surface center; see Fig. 3(b). In this case, the spatial distribution of the emission follows a Gaussian distribution if the loss caused by the center electrode is not considered [the pixels are saturated in Fig. 3(b)]. The video in Appendix B (Visualization 1) shows the evolution of the emission intensity profile as the LED is electrically pumped across the threshold

current. Together with the above results, including the behavior of the emission energy, FWHM, intensity, and integral intensity, this observation confirms the presence of electrically driven stimulated emission, although it lacks a suitable cavity [31–33].

### C. Carrier Relaxation Dynamics by Time-Resolved PL

We now address the electronic structure of the  $\text{Er}^{3+}$ -doped Si and the carrier relaxation and transfer dynamics. Figure 4(a) shows the TR-PL results under a pulsed laser excitation ( $\lambda = 760$  nm, 80 MHz) at 5 K. The recorded PL signals are between 1.1 and 1.2 eV. On the time scale, the PL amplitudes remain nearly constant at a scale of  $\sim 12$  ns, indicating that the emission has a longer lifetime. The time-integrated PL spectrum can be fitted with a Gaussian distribution with a peak centered at  $\sim 1.15$  eV, as shown in Fig. 4(b), which likely comes from the band-to-band emission in Si [39]. The corresponding decay profile shown in Fig. 4(c) suggests that the lifetime is much longer than  $\sim 12$  ns, consistent with the picture presented in Fig. 4(a). Notice that the streak camera used is not capable of detecting light near  $\sim 1.5$   $\mu\text{m}$  in wavelength and that the time resolution is better than 10 ps; also see Fig. 4(c).

When the frequency-doubled wavelength (380 nm) excites the sample, a similar but smaller emission band at  $\sim 1.15$  eV was observed; see Fig. 4(d). In the time domain, the emission has two striking features shown in Fig. 4(e). First, unlike the long emission lifetime excited at the wavelength of 760 nm, the emission has a short decay time of  $\sim 30$  ps. Second, the emission lags behind the excitation pulse by  $\sim 110$  ps. These features are likely caused by the fact that high-energy photons from the

380 nm laser can excite electrons from the VB to the L (or  $\Gamma'$ ) point of the CB, which the 760 nm laser excitation cannot do. With assistance of phonons, hot electrons from the L point will first transit to the CB bottom ( $\Delta_{1c}$  point) and then emit photons at  $\sim 1.15$  eV via radiative recombination from band to band. It should be emphasized that the time difference of  $\sim 110$  ps cannot be the coupling-related error of the test system, since the drift of the system, i.e., the desynchronization, is about 5 ps per hour in the synchro-scan regime. It could be then attributed to the transfer time of the carriers across the intravalley barrier. The relatively long transit time results in a low concentration of excess carriers at the CB bottom because the barrier temporally holds the carriers at the L point. As a result, excess carriers do not generate strong spontaneous emission but rapidly ( $\sim 30$  ps) relax to the Er/O-related quasi-continuous levels below the indirect CB of Si [15,16]; see more discussion later. This behavior is illustrated by the blue transients in Fig. 4(e). This fast relaxation process suggests a fundamental discrepancy with the existing model of energy transfer from electron-hole pair recombination directly to the excitation of the  $\text{Er}^{3+}$ -4f electrons for the  $1.54$   $\mu\text{m}$  emission [40].

The analysis of all these findings results in a comprehensive picture, which is shown schematically in Fig. 5. High-energy photons from the 380 nm laser first excite electrons from the VB to the L point of the CB. Due to the intervalley barriers, these carriers slowly transit to the bottom of the indirect CB ( $\Delta_{1c}$ ) with a time constant of  $\sim 110$  ps. Since the localized states in the quasi-continuous Er/O-related donor band have larger momentum, excess carriers at the indirect CB bottom can be readily coupled and transferred to the Er/O-related donor band with a relatively short lifetime of  $\sim 30$  ps. Finally, the carriers relax to the VB via radiative and nonradiative recombination in the quasi-continuous Er/O-related donor band. The radiative recombination broadens the emission band up to the Si band gap, and the nonradiative recombination mainly transfers energy to resonantly excite the  $\text{Er}^{3+}$ . Thus, the quasi-continuous band not only facilitates the rapid emission decay of  $\sim 30$  ps (by 380 nm laser excitation) shown in Fig. 4(e) but

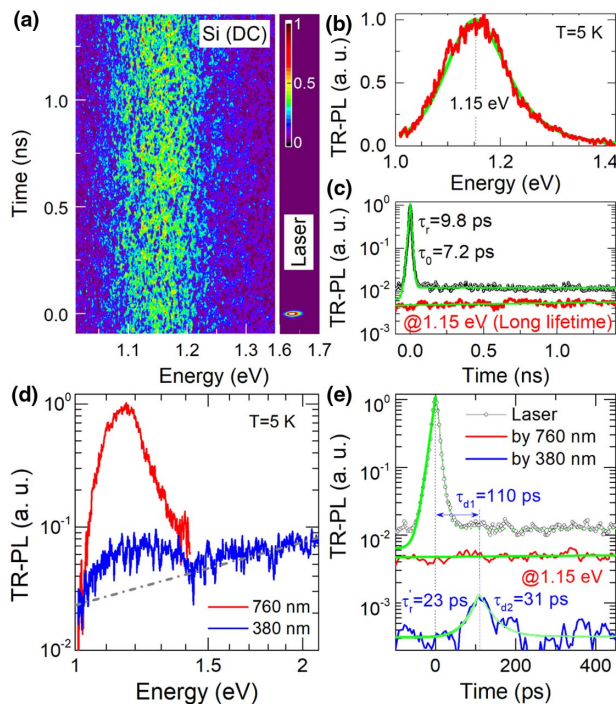


**Fig. 4.** TR-PL spectral results. (a) TR-PL image from the Er/O-doped Si at 5 K (left) with a 760 nm excitation laser. (b) Time-integrated spectrum and Gaussian fit. (c) Decay curves of the sample and the laser. (d) Time-integrated spectra at excitation wavelengths of 760 and 380 nm. (e) Decay curves at different excitation wavelengths.

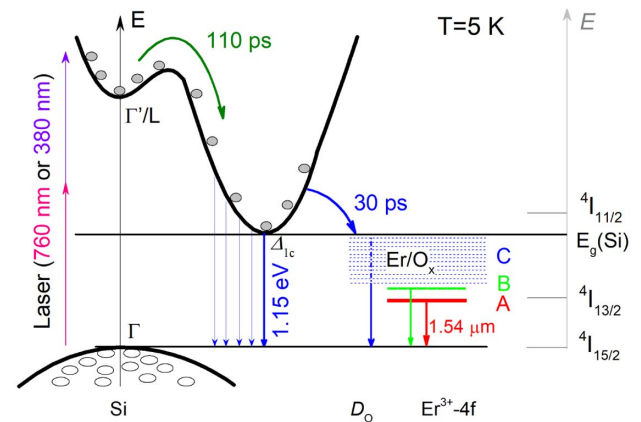


**Fig. 5.** Scheme of the carrier relaxation dynamics. The hot carriers in the upper states at  $\Gamma'$  or L points excited by the 380 nm laser transfer to the indirect CB minimum ( $\Delta_{1c}$ ) of Si with a time constant of  $\sim 110$  ps. From here, a time constant of  $\sim 30$  ps characterizes the transition of carriers to the distributed band created by the Er/O-related donor states.

also serves as efficient nonradiation recombination centers to resonantly excite the  $\text{Er}^{3+}$  for the  $1.54\ \mu\text{m}$  emission. This could be one of the reasons why the  $1.54\ \mu\text{m}$  emission in Er/O-doped Si is usually not effectively excited by infrared photons but by high-energy photons, e.g.,  $\sim 400\ \text{nm}$ , which then produce the amplified emission. Although the fast relaxation of carriers within the quasi-continuous donor band cannot be directly detected, the extremely long lifetime of the  $\text{Er}^{3+}$  emission at  $1.54\ \mu\text{m}$  ( $\sim \text{ms}$ ) facilitates the achievement of inversion, resulting in amplified spontaneous (or stimulated) emission. The main reason why it is complicated to obtain amplified emission by optical excitation (i.e., PL) is the high reflectance loss of visible light at the surface of the polished Si matrix. Although the temperature shows no influence on the reflectivity, the loss of surface reflectivity is high (e.g.,  $\sim 40\%$  for  $405\ \text{nm}$ ) [41]; also see Fig. 8 in Appendix C.

Notice that the  $\text{Er}^{3+}$  sublevels of excited and ground states have an energy separation of about  $10\text{--}15\ \text{meV}$  between the first-lying and second-lying crystal field split levels of the first ( $^4\text{I}_{13/2}$ ) excited state [40]. Since the activation energy for band A ( $1.54\ \mu\text{m}$ ) is  $14.9\ \text{meV}$  and the electrons in band A are thermally excited to band B as shown in Fig. 1(e), the emission center of bands A and B is likely related to the first-lying and the second-lying split levels of  $^4\text{I}_{13/2}$  and to the sublevels of ( $^4\text{I}_{15/2}$ ) the ground state, respectively. As for the activation energy of  $\sim 40\ \text{meV}$  for the entire emission signal in this material system, it can be tentatively ascribed to the co-contributions of the reversed transfer of the nonequilibrium carriers from the impurity-related band C to the Si and the potential nonradiative recombination of carriers of band C via electron-phonon coupling.

What needs to be emphasized again is that the results achieved are largely due to the use of the DC process in sample preparation. The process offers advantages for the optically pumped  $\text{Er}^{3+}$ . These ions appear in high density in relatively uniformly sized, Er-related clusters with a diameter of  $\sim 1\ \text{nm}$ , which is much smaller than the  $5\ \text{nm}$  diameter achieved with the standard RTA process [11]. Moreover, the spatial distribution of the small clusters is extremely even, which provides very useful conditions for the Er/O cluster to act as a broad and quasi-continuous donor band [42]. The decaying carriers from the Si host into the Er-related states excite the  $4f$  electron of  $\text{Er}^{3+}$ , which produces the emission at  $\sim 1.54\ \mu\text{m}$ . Details on material characterizations by high-resolution transmission electron microscopy and X-ray photoelectron spectroscopy have been described in Ref. [11], and the striking difference of the defect-related PL signal between RTA and DC is shown in Fig. 9 in Appendix C.

#### 4. CONCLUSIONS

In conclusion, we observed amplified spontaneous (or stimulated) emissions at room temperature with a low threshold of  $\sim 0.8\ \text{A}/\text{cm}^2$  from Er/O-doped Si-based LEDs that were treated with a DC process. In comparison with the standard RTA process, the DC process can effectively suppress the precipitation of Er/O-related nanocrystals and form more uniformly distributed Er-O-Si compounds. The impact of the DC process on Er/O formation can effectively reduce the

density of nonradiative defects in the Si band gap and facilitate the formation of a quasi-continuous Er/O-related donor band right below the Si CB. As a result, strong room-temperature PL and amplified spontaneous (or stimulated) emissions were directly observed for them. In particular, the quasi-continuous Er/O-related donor band not only facilitates the rapid emission decay of excess carriers but also serves as efficient recombination centers to extend the emissions up to the Si band gap, forming a broad tail in the spectrum in addition to the widely observed  $\text{Er}^{3+}$  emission at  $1.54\ \mu\text{m}$ . This work may pave the way for fabricating superluminescent (or laser) diodes at communication wavelengths based on rare-earth-doped silicon.

#### APPENDIX A: SCHEMATIC OF THE FABRICATION PROCEDURE

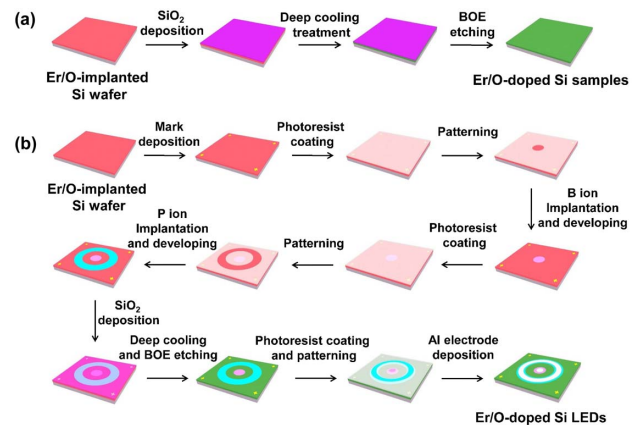


**Fig. 6.** Schematic representation of the fabrication procedure to form (a) Er/O-doped Si samples and (b) LED devices.

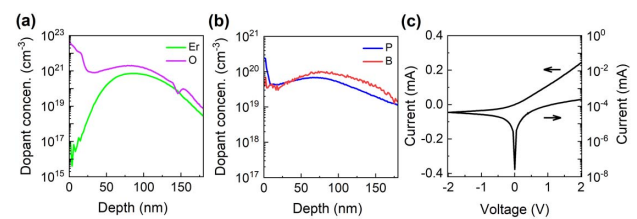


**Fig. 7.** Concentration and electrical characterization of Er/O-doped Si LEDs. (a) Erbium (green line) and oxygen (purple line) and (b) boron (red line) and phosphorous (blue line) ion distribution profiles on their respective implantation region of Er/O-doped Si devices by secondary ion mass spectroscopy (SIMS) measurement. (c)  $I - V$  curves of the diode devices.

#### APPENDIX B: NEAR-INFRARED EL IMAGING FROM THE Er/O-Si LEDs

This video ([Visualization 1](#)) clearly shows the narrowing of the intensity distribution of the EL with current increase as discussed in the text.



## APPENDIX C: COMPARISON OF TRANSMISSION, REFLECTANCE, AND NORMALIZED PL SPECTRA OF Er-DOPED Si SAMPLES BY RTA AND DC PROCESSES

Figures 8(a) and 8(b) show that the surface polishing of Si has almost no influence on the transmittance at room temperature. The Er doping causes a  $\sim 10\%$  decrease of the transmittance below the band gap of Si, but the DC technique does not affect the transmission results of the Si host. Note that for Er doping, the injection surface of the Si is always fine polished.

Figure 8(c) shows that the transmission of the Er-doped Si samples obtained by the DC technique, e.g., at 405 nm, is independent of temperature, which is cross-checked by the corresponding absorption coefficient spectra in the inset.

Figure 8(d) reveals that the fine polishing of the Si surface can enhance the reflectivity of the Si by  $\sim 13\%$ . Notice that the reflectivity of the fine-polished Si surface can increase due to the Er doping, but the DC technique makes the reflectivity of the Er-doped Si decrease substantially toward the short-wavelength side, e.g., from  $\sim 55\%$  to  $\sim 40\%$  at 405 nm. It should be pointed out that the loss of almost half of the incident photons of 405 nm (i.e.,  $\sim 40\%$  reflectivity of the Er-doped Si surface at 405 nm) shows the disadvantage with respect to the quantum efficiency when short-wavelength excitation is required. This may be the reason why the amplified spontaneous (or stimulated) emission can be observed by EL rather than by PL.

Figure 9 shows that, together with the Er-related PL feature at  $\sim 0.81$  eV ( $\sim 1.54$   $\mu\text{m}$ ), a shoulder at the high-energy side can be observed in the DC processed sample. As a comparison, the samples by the RTA process only show the Er-related PL feature with the shoulder at the high-energy side at 5 K

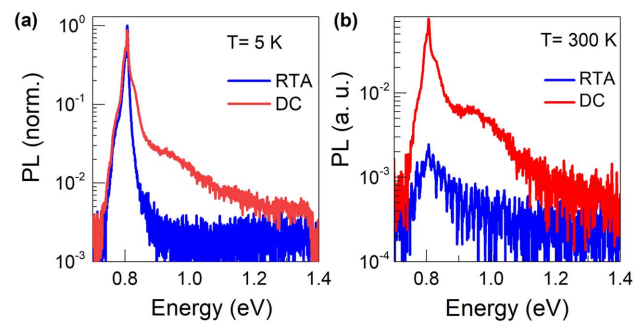


**Fig. 9.** Comparison of normalized PL spectra of Er-doped Si samples by RTA and DC processes in a semi-logarithmic plot (a) at 5 K and (b) at 300 K.

[Fig. 9(a)], but it becomes extremely weakened when the temperature increases to 300 K [Fig. 9(b)]. It is also clear that the PL signal is extremely low and does not show the Er-related PL feature. Note that broad quasi-continuous states act as an important channel for the transfer of carriers from the high-energy states to the  $\text{Er}^{3+}$ , although they simultaneously contribute to radiative recombination.

**Funding.** National Natural Science Foundation of China (61790583, 61874043, 61874072, 21703140); Special-key project of the “Innovative Research Plan”, Shanghai Municipality Bureau of Education (2019-01-07-00-02-E00075); Aero-Science Fund (201824X001).

**Acknowledgment.** The authors thank Dr. Ren Zhu for the characterization of spatially resolved intensity distribution at the emitting surface of the LED.

**Disclosures.** The authors declare no conflicts of interest.

<sup>†</sup>These authors contributed equally to this paper.

## REFERENCES

1. X. Chen, M. M. Milosevic, S. Stanković, S. Reynolds, T. D. Bucio, K. Li, D. J. Thomson, F. Gardes, and G. T. Reed, “The emergence of silicon photonics as a flexible technology platform,” *Proc. IEEE* **106**, 2101–2116 (2018).
2. D. Thomson, A. Zilkie, J. E. Bowers, T. Komljenovic, G. T. Reed, L. Vivien, D. Marris-Morini, E. Cassan, L. Viot, and J.-M. Fédéli, “Roadmap on silicon photonics,” *J. Opt.* **18**, 073003 (2016).
3. Z. Zhou, B. Yin, and J. Michel, “On-chip light sources for silicon photonics,” *Light Sci. Appl.* **4**, e358 (2015).
4. H. Subbaraman, X. Xu, A. Hosseini, X. Zhang, Y. Zhang, D. Kwong, and R. T. Chen, “Recent advances in silicon-based passive and active optical interconnects,” *Opt. Express* **23**, 2487–2511 (2015).
5. D. Liang and J. E. Bowers, “Recent progress in lasers on silicon,” *Nat. Photonics* **4**, 511–517 (2010).
6. D. A. Miller, “Device requirements for optical interconnects to silicon chips,” *Proc. IEEE* **97**, 1166–1185 (2009).
7. E. M. Fadaly, A. Dijkstra, J. R. Suckert, D. Ziss, M. A. van Tilburg, C. Mao, Y. Ren, V. T. van Lange, K. Korzun, and S. Kölling, “Direct-bandgap emission from hexagonal Ge and SiGe alloys,” *Nature* **580**, 205–209 (2020).
8. C. Roques-Carnes, S. E. Kooi, Y. Yang, A. Massuda, P. D. Keathley, A. Zaidi, Y. Yang, J. D. Joannopoulos, K. K. Berggren, and I. Kaminer,

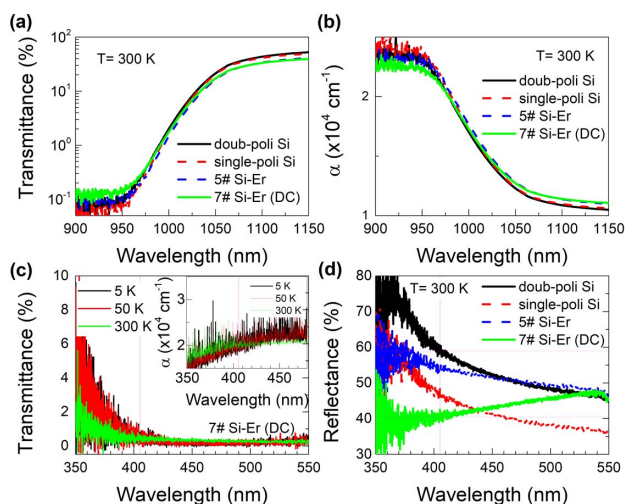


**Fig. 8.** Transmission and reflectance spectra of the Er-doped Si with or without application of the DC technique at 300 K. For comparison, the results of the pure Si after double-side polish or single-side polish are also shown. (a) The transmission spectra of the polished-pure and Er-doped Si at 300 K; (b) the corresponding absorption coefficient spectra from (a); (c) the transmission spectra of the Er-doped Si obtained by the DC technique at different temperatures; (d) the reflectance spectra.

- "Towards integrated tunable all-silicon free-electron light sources," *Nat. Commun.* **10**, 3176 (2019).
9. S. Chen, W. Li, J. Wu, Q. Jiang, M. Tang, S. Shutts, S. N. Elliott, A. Sobiesierski, A. J. Seeds, and I. Ross, "Electrically pumped continuous-wave III–V quantum dot lasers on silicon," *Nat. Photonics* **10**, 307–311 (2016).
  10. Y. Takahashi, Y. Inui, M. Chihara, T. Asano, R. Terawaki, and S. Noda, "A micrometre-scale Raman silicon laser with a microwatt threshold," *Nature* **498**, 470–474 (2013).
  11. H. Wen, J. He, J. Hong, S. Jin, Z. Xu, H. Zhu, J. Liu, G. Sha, F. Yue, and Y. Dan, "Efficient Er/O-doped silicon light-emitting diodes at communication wavelength by deep cooling," *Adv. Opt. Mater.* **8**, 2000720 (2020).
  12. M. A. Hughes, H. Li, N. Theodoropoulou, and J. D. Carey, "Optically modulated magnetic resonance of erbium implanted silicon," *Sci. Rep.* **9**, 1 (2019).
  13. M. Celebrano, L. Ghirardini, M. Finazzi, G. Ferrari, Y. Chiba, A. Abdelghafar, M. Yano, T. Shinada, T. Tani, and E. Prati, "Room temperature resonant photocurrent in an erbium low-doped silicon transistor at telecom wavelength," *Nanomaterials* **9**, 416 (2019).
  14. M. Lourenço, M. Milošević, A. Gorin, R. Gwilliam, and K. Homewood, "Super-enhancement of 1.54  $\mu\text{m}$  emission from erbium co-doped with oxygen in silicon-on-insulator," *Sci. Rep.* **6**, 1 (2016).
  15. A. Kenyon, "Erbium in silicon," *Semicond. Sci. Tech.* **20**, R65–R84 (2005).
  16. N. Q. Vinh, N. N. Ha, and T. Gregorkiewicz, "Photonic properties of Er-doped crystalline silicon," *Proc. IEEE* **97**, 1269–1283 (2009).
  17. G. Franzò, F. Priolo, and S. Coffa, "Understanding and control of the erbium non-radiative de-excitation processes in silicon," *J. Lumin.* **80**, 19–28 (1998).
  18. H. Shen, D.-S. Li, and D.-R. Yang, "Research progress of silicon light source," *Acta Phys. Sin.* **64**, 204208 (2015).
  19. S. Wu, S. Buckley, J. R. Schaibley, L. Feng, J. Yan, D. G. Mandrus, F. Hatami, W. Yao, J. Vučković, and A. Majumdar, "Monolayer semiconductor nanocavity lasers with ultralow thresholds," *Nature* **520**, 69–72 (2015).
  20. J. Hong, H. Wang, F. Yue, J. W. Tamm, D. Kruschke, C. Jing, S. Chen, Y. Chen, W. Hu, and J. Chu, "Emission kinetics from PbSe quantum dots in glass matrix at high excitation levels," *Phys. Status Solidi R* **12**, 1870312 (2018).
  21. J. Ramírez, F. F. Lupi, Y. Berencén, A. Anopchenko, J. Colonna, O. Jambois, J. Fedeli, L. Pavesi, N. Prtljaga, and P. Rivallin, "Er-doped light emitting slot waveguides monolithically integrated in a silicon photonic chip," *Nanotechnology* **24**, 115202 (2013).
  22. T. Kobayashi, M. Djiango, and W. J. Blau, "Near-infrared electroluminescence and stimulated emission from semiconducting nonconjugated polymer thin films," *J. Appl. Phys.* **107**, 023103 (2010).
  23. V. Ho, Y. Wang, B. Ryan, L. Patrick, H. Jiang, J. Lin, and N. Vinh, "Observation of optical gain in Er-doped GaN epilayers," *J. Lumin.* **221**, 117090 (2020).
  24. N. T. Otterstrom, R. O. Behunin, E. A. Kittlaus, Z. Wang, and P. T. Rakich, "A silicon Brillouin laser," *Science* **360**, 1113–1116 (2018).
  25. H. Liu, Z. Li, W. Song, Y. Yu, F. Pang, and T. Wang, "MoS<sub>2</sub>/graphene heterostructure incorporated passively mode-locked fiber laser: from anomalous to normal average dispersion," *Opt. Mater. Express* **10**, 46–56 (2020).
  26. S. Saito, T. Takahama, K. Tani, M. Takahashi, T. Mine, Y. Suwa, and D. Hisamoto, "Stimulated emission of near-infrared radiation in silicon fin light-emitting diode," *Appl. Phys. Lett.* **98**, 261104 (2011).
  27. V. Robbiano, G. M. Paternó, A. A. La Mattina, S. G. Motti, G. Lanzani, F. Scotognella, and G. Barillaro, "Room-temperature low-threshold lasing from monolithically integrated nanostructured porous silicon hybrid microcavities," *ACS Nano* **12**, 4536–4544 (2018).
  28. K. Luterová, D. Navarro, M. Cazzanelli, T. Ostatnický, J. Valenta, S. Cheylan, I. Pelant, and L. Pavesi, "Stimulated emission in the active planar optical waveguide made of silicon nanocrystals," *Phys. Status Solidi C* **2**, 3429–3434 (2005).
  29. A. Rapaport and M. Bass, "The role of stimulated emission in luminescence decay," *J. Lumin.* **97**, 180–189 (2002).
  30. M. Bresler, O. Gusev, E. Terukov, I. Yassievich, B. Zakharchenya, V. Emel'yanov, B. Kamenev, P. Kashkarov, E. Konstantinova, and V. Y. Timoshenko, "Stimulated emission in erbium-doped silicon structures under optical pumping," *Mater. Sci. Eng. B* **81**, 52–55 (2001).
  31. L. A. Coldren, S. W. Corzine, and M. L. Mashanovitch, *Diode Lasers and Photonic Integrated Circuits* (Wiley, 2012), Vol. **218**.
  32. V. Ho, T. A. Tahtamouni, H. Jiang, J. Lin, J. Zavada, and N. Vinh, "Room-temperature lasing action in GaN quantum wells in the infrared 1.5  $\mu\text{m}$  region," *ACS Photon.* **5**, 1303–1309 (2018).
  33. M. Huda and S. Ali, "A study on stimulated emission from erbium in silicon," *Mater. Sci. Eng. B* **105**, 146–149 (2003).
  34. M. Schultze, K. Ramasesha, C. Pemmaraju, S. Sato, D. Whitmore, A. Gandman, J. S. Prell, L. Borja, D. Prendergast, and K. Yabana, "Attosecond band-gap dynamics in silicon," *Science* **346**, 1348–1352 (2014).
  35. J. Noffsinger, E. Kioupakis, C. G. Van de Walle, S. G. Louie, and M. L. Cohen, "Phonon-assisted optical absorption in silicon from first principles," *Phys. Rev. Lett.* **108**, 167402 (2012).
  36. X. Wang, B. Wang, L. Wang, R. Guo, H. Isshiki, T. Kimura, and Z. Zhou, "Extraordinary infrared photoluminescence efficiency of Er<sub>0.1</sub>Yb<sub>0.9</sub>SiO<sub>5</sub> films on SiO<sub>2</sub>/Si substrates," *Appl. Phys. Lett.* **98**, 071903 (2011).
  37. B. De Geyter, A. J. Houtepen, S. Carrillo, P. Geiregat, Y. Gao, S. t. Cate, J. M. Schins, D. Van Thourhout, C. Delerue, and L. D. Siebbeles, "Broadband and picosecond intraband absorption in lead-based colloidal quantum dots," *ACS Nano* **6**, 6067–6074 (2012).
  38. W. J. Miniscalco and R. S. Quimby, "General procedure for the analysis of Er<sup>3+</sup> cross sections," *Opt. Lett.* **16**, 258–260 (1991).
  39. W. L. Ng, M. Lourenco, R. Gwilliam, S. Ledain, G. Shao, and K. Homewood, "An efficient room-temperature silicon-based light-emitting diode," *Nature* **410**, 192–194 (2001).
  40. V. X. Ho, T. V. Dao, H. X. Jiang, J. Y. Lin, J. M. Zavada, S. A. McGill, and N. Q. Vinh, "Photoluminescence quantum efficiency of Er optical centers in GaN epilayers," *Sci. Rep.* **7**, 1 (2017).
  41. I. Costa, D. Pera, and J. A. Silva, "Improving light capture on crystalline silicon wafers," *Mater. Lett.* **272**, 127825 (2020).
  42. M. Bürkle, M. Lozac'h, C. McDonald, M. Macias-Montero, B. Alessi, D. Mariotti, and V. Švrček, "Tuning the bandgap character of quantum-confined Si-Sn alloyed nanocrystals," *Adv. Funct. Mater.* **30**, 1907210 (2020).